Biochar aerogel decorated with thiophene S manipulated 5-membered rings boosts nitrogen fixation

Xiaokang Chen [a],[1], Lijie Zhang [a],[1], Wenjia Xu [a], Xin Ding [a], Shuai Chen [b], Xilin She [a], Xiangxin Guo [a], Chung-Li Dong [c], Yucheng Huang [c], Lixue Zhang [a], Shaohua Shen [d], Dongjiang Yang [a],[e],[*]

[a] State Key Laboratory of Bio-fibers and Eco-textiles, Shandong Collaborative Innovation Center of Marine Bio-Based Fibers and Ecological Textiles, Institute of Marine Biobased Materials, College of Environmental Science and Engineering, Qingdao University, Qingdao 266071, PR China
[b] State Key Laboratory of Coal Conversion, Institute of Coal Chemistry Chinese Academy of Science, Taiyuan 030001, PR China
[c] Research Center for X-ray Science, Department of Physics, Tamkang University, Tamsui 25137, Taiwan
[d] State Key Laboratory of Multiphase Flow in Power Engineering, International Research Center for Renewable Energy, Xi'an Jiaotong University, Xi'an 710049, PR China
[e] Queensland Micro, and Nanotechnology Centre (QMNC), Griffith University, Nathan, Brisbane, Queensland 4111, Australia

ARTICLE INFO

ABSTRACT

Algae contains most of the marine biogenic S, and is the main producer of dimethylsulfide, of which oxidation products contribute ~ 40% acidity of the acid rain. The biogenic S of red algae mainly exists in carrageenan molecules. In this work, 89% of C and 96% of biogenic S in carrageenan was synchronically fixed into biochar to form thiophene S decorated biochar aerogel (SCA), efficiently preventing the loss of C and S elements. More importantly, the presence of thiophene S structure in SCA can "push" electrons into the antibonding orbitals of N_2, and simultaneously "pull" the lone-pair electrons from N_2, thus endowing the SCA super activity for nitrogen reduction reaction. Experimentally, its NH_3 yield rate reaches high as 36.69 μg h^{-1} mg_{cat}^{-1}, surpassing most metal-free electrocatalysts. Theoretical calculations demonstrate that the thiophene S can promote the absorption and activation of N_2, and efficiently lower the energy barrier of N_2 protonation.

1. Introduction

Sulfur (S) cycle is a process of transformation and reciprocation of the S elements in the ecosystem and environment (Fig. S1), wherein the acid rain is a big problem due to its great harm to ecological environment, agriculture and even human beings [1,2]. Algae, which contains most of the marine biogenic sulfur (S), is the main producer of dimethylsulfide (DMS), of which the oxidation products contributes ~ 40% of the acidity of acid rain [3,4]. In red algae, most of the biogenic S is found in polymers called carrageenan, which contains a large number of sulfonic groups [5]. Carrageenan has the properties of temperature-sensitive gel, and its molecular chain will show "spiral" transformation during the cooling process. The carrageenan with "spiral" molecular chains has potential to generate three-dimensional (3D) hierarchical porous biochar aerogels [6]. Recently, biochar materials and

their applications in emerging energy storage and conversion have become an attractive topic in the field of sustainable development [7,8]. The utilization of biochar materials could play the role of carbon sequestration and carbon reduction, and greatly reduce the emission of CO_2, which is an effective way to mitigate global warming [9]. In addition, the introduction of S into biochar can endow the carbon aerogel superior electrocatalysis activity by regulating the charge density of adjacent C atoms [10,11], and thus improve the added value of biochar materials. Therefore, large-scale utilization of carrageenan to synthesize biochar can not only play an important role in fixing S and C, but also provide an excellent electrocatalyst for advanced energy conversion.

Ammonia (NH_3) is one of the most important fundamental chemicals for humans [12–16]. Since Davy et al. discovered the electrochemical N_2 reduction reaction (NRR), it has become a promising alternative to traditional industrial ammonia synthesis (Haber-Bosch) approach for

---

the synthesis of NH_3 [17–21]. Compared to traditional Haber-Bosch process, the electrocatalytic process using the sustainable protons in water to replace the hydrogen gas used in industry, and convert N_2 into NH_3 by controlling the potential, which greatly reduces energy consumption and carbon dioxide emissions, and promote the sustainable development of human society [22–26]. However, the chemical super-stability of N_2 molecules make the realization of electrocatalytic NRR difficult, which requires the search of catalysts with special active sites to accelerate ammonia synthesis [27–29]. The designed NRR electro-catalysts should exhibit excellent apparent activity to efficiently pro-mote the diffusion of solvated gas (N_2) and electrolytes, and exhibit outstanding intrinsic activity to improve the catalytic ability of active sites, thus accelerating the cleavage and protonation of N_2 to enhance the activity of NRR [30,31]. Biochar aerogels is of high potential for catalyzing NRR owing to the large surface area and highly porous structure, which expose more catalytic sites and facilitate the diffusion of reactants and electrolytes [32,33]. Besides, the introduction of het-eroatom into biochar could regulate the charge density of adjacent C atoms and accelerate the N_2 protonation, thereby enhancing the NRR performances [34,35].

Herein, we fabricated biochar aerogel electrocatalysts decorated with thiophene S (SCA) for electrochemical NRR by directly pyrolyzing carrageenan. During this process, 89% carbon was retained and con-verted to biochar structure. Meanwhile, 96% marine biogenic S was cured to thiophene S and oxidized S species into the biochar, efficiently preventing the loss of S element. More importantly, the thiophene S structure in the SCA achieves excellent electrochemical N_2 reduction reaction (NRR) performance with a highest NH_3 yield rate of 36.69 µg h^{-1} mg_{cat}^{-1} and Faradaic efficiency (FE) of 8.72% in acid solution under ambient conditions. Density functional theory (DFT) calculation results further confirm that thiophene S structure can effectively regulate the charge density of adjacent C atoms, and facilitate the adsorption, dissociation and protonation of N_2 molecules on carbon substrate, thus reducing the energy barrier for NRR. The preferable reaction pathway for NRR is N_2 (g) $\rightarrow NN^* \rightarrow NNH^* \rightarrow NNH_2^* \rightarrow N^* \rightarrow NH^* \rightarrow NH_2^* \rightarrow NH_3^*$.

2. Experimental section

2.1. Synthesis of SCA-700

Firstly, 2 g iota-carrageenan powder was dispersed in 100 mL of deionized water using the magnetic stirring for 1 h at 80 °C, and the obtained solution was cooled to room-temperature, forming a carra-geenan hydrogel. Then, the hydrogel was freezen dried to obtain carrageenan aerogel. Thirdly, the carrageenan aerogel was pyrolyzed at 700 °C at a heating rate of 5 °C min^{-1} for 2 h in Ar atmosphere. Finally, the pyrolyzed sample was leached by 3 M HCl solution at 70 °C, and the as-obtained SCA-700 was collected by filtration and washed with deionized water several times.The synthesis process of SCA-600 and SCA-800 are similar to the above method of SCA-700, except for the pyrolysis temperature.

2.2. Synthesis of SCA-700–1100

The as-synthesized SCA-700 was annealed at 1100 °C for 1 h under Ar atmosphere to remove most of S atoms, and the obtained samples was denoted as SCA-700–1100.

2.3. Characterizations and methods

The details of Material Characterizations, Electrochemical NRR Measurements, Determination of Ammonia, Determination of Hydra-zine, Computation methods and detail and $^{15}N_2$ isotope labelling ex-periments are provided in Supplementary Material.

3. Results and discussion

3.1. Preparation of SCA

As illustrated in Fig. 1, the S element in ɩ−carrageenan was fixed in the SCA framework and converted to thiophene S and oxidized S species by using a simple freeze−drying and pyrolysis process. Specifically, the hot aqueous carrageenan solution converted to transparent hydrogel after cooling down at a temperature lower than 80 °C, since the random coiled carrageenan macromolecules were cross−linked to form "dou-ble−helix" structure [36]. After subsequent freeze−drying, the carra-geenan hydrogel converted to highly porous aerogel. Finally, the carrageenan aerogel was pyrolyzed at T °C (600, 700, and 800) under Ar atmosphere to obtain ultralight S−doped carbon aerogels (SCA−T). Besides, the inductively coupled plasma atomic emission spectroscopy (ICP-AES) also was performed to prove that no common metals existed in SCA electrocatalyst (Table S1).

3.2. Morphology and structure of SCA

Fig. 2a displays the X − ray diffraction (XRD) patterns of as−synthesized SCA−T. The two diffraction peaks (23.0 and 43.5°) are assigned to the (002) and (101) diffraction plane of graphitic structure in SCA matrix. The N_2 adsorption−desorption isotherms and pore size distribution of SCA−T are shown in Fig. 2b and c. The adsorption occurred at the relative pressure ($P / P_0 < 0.02$) indicates the existence of micropores in the samples. The H4 −type hysteresis loop originates from the presence of mesopores [37]. The SCA− 700 owns the highest Brunauer–Emmett–Teller (BET) surface area (1668.9 m^2 g^{-1}), which is much higher that that of SCA-600 (990.6 m^2 g^{-1}) and SCA-800 (1063.8 m^2 g^{-1}). From the pore size distribution, the pore diameters are located at $\sim$ 1.0 nm (micropores) and $\sim$ 2.3 nm (small mesopores) by the desorption branch of isotherm calculation. The appearance of micropores and mesopores in SCA−T is due to the decomposition of sulfur and oxygen groups ($-SO_4H$, $-COOH$, and $-OH$) in carrageenan macromolecules. The high BET surface area combined with hierarchical porous structure could efficiently promote the diffusion of solvated gas (N_2) and electrolytes, thus accelerating the protonation of N_2 to enhance the activity of NRR [31]. The as−synthesized samples were character-ized by using scanning electron microscopy (SEM) and transmission electron microscopy (TEM), which were displayed in the SEM and TEM images (Fig. 2d, e and f). Obviously, the SCA is a 3D self−supporting porous network structure. A large amount of macropores, mesopores (25 −50 nm) and micropores can be observed on the surface of SCA, which is consistent with the above results of pore size distribution. The mesopores and micropores can provide large electrode/electrolyte interface to accelerate electron transfer [38,39]. EDS mapping spectrum indicates that C, S and O elements are uniformly dispersed in the whole SCA (Fig. 2g).

3.3. Thermogravimetric analysis of Carrageenan aerogel

The thermogravimetric analysis (TG/DTG) and the corresponding mass spectra (TG-MS) were carried out to reveal the pyrolysis process of carrageenan aerogel. The DTG curve shows three more distinct stages of heat gains at 207 °C, 310 °C and 726 °C during the whole pyrolysis process. Meanwhile, the first, second and third major weight loss steps could be found in the TG curve, that occur in the temperature range of 190 − 221 °C, 227 − 380 °C and 672 − 741 °C, respectively (Fig. 3a). As shown in the Fig. 3b, the corresponding TG-MS curves display the volatiles from aerogel pyrolysis are CO_2 (m/z: 44), H_2O (m/z: 18), SO_2 (m/z: 64) and CO (m/z: 28). The sharp peaks could be found at the temperature of 194 °C from the pink and purple curves (H_2O and CO_2), respectively, which corresponds to the first rapid weight loss step (190 −221 °C) of the TG curve. Besides, the peaks at 296 °C in pink and orange curves (CO_2 and SO_2), and the peaks at 700 °C in pink and olive
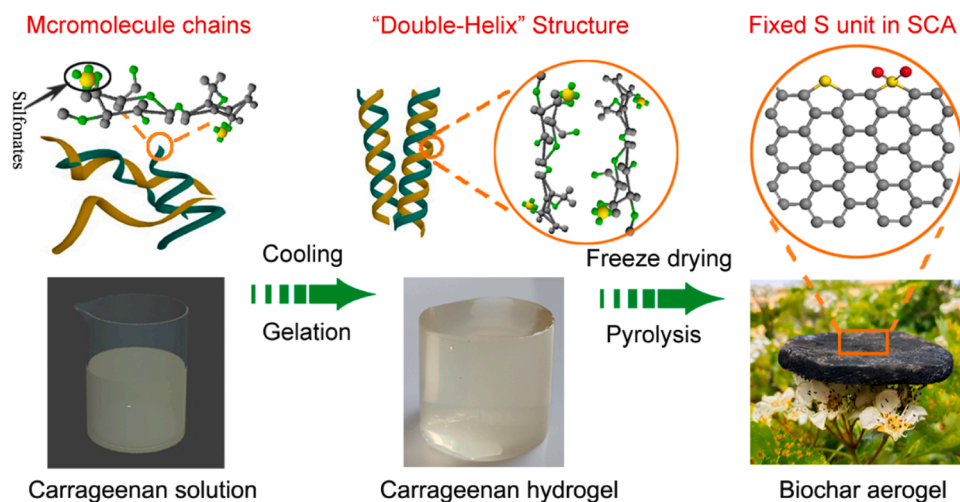
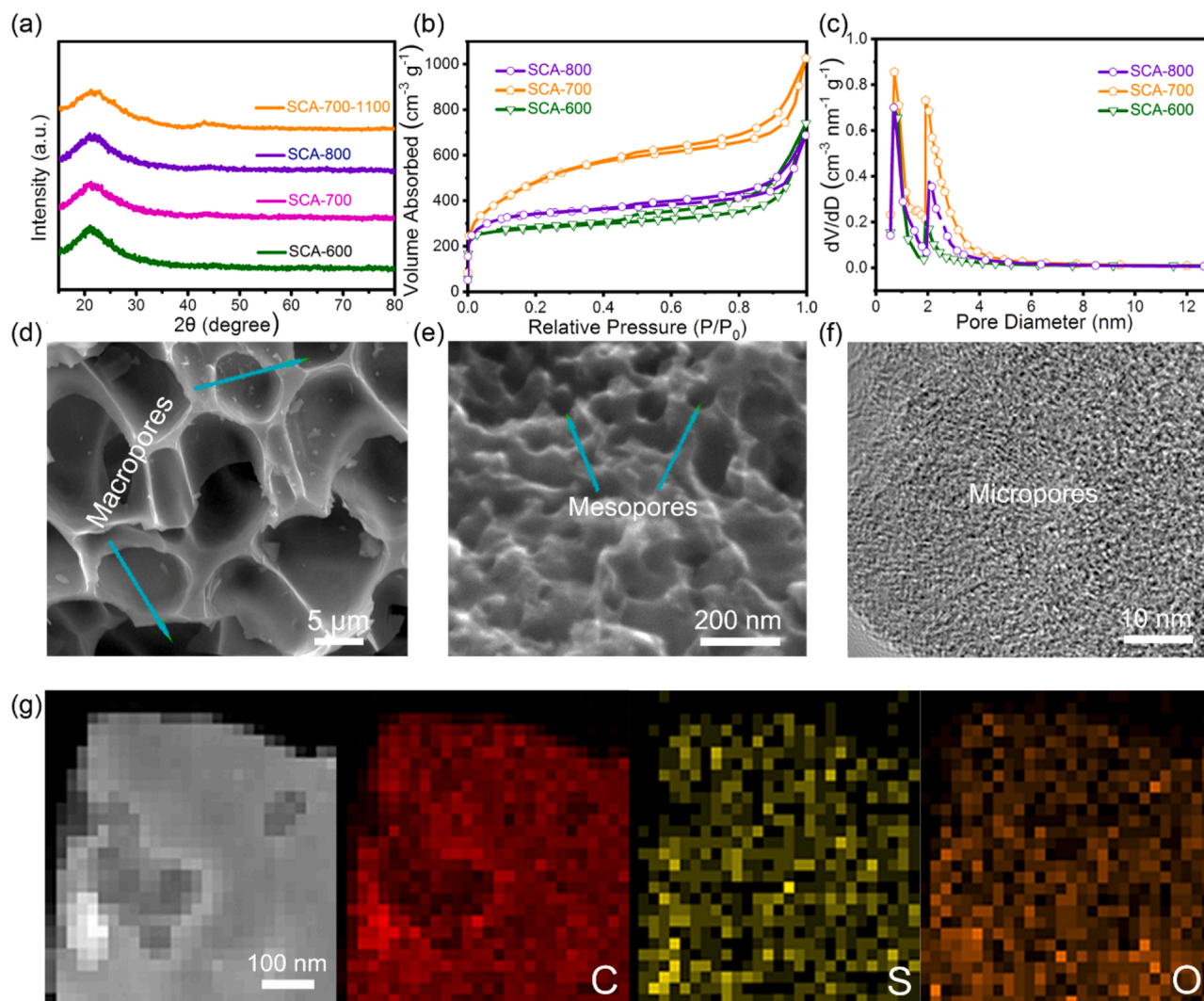**Fig. 1.** Schematic illustration of marine biogenic S fixation.

Fig. 2. (a) XRD patterns of SCA−T. (b-c) Nitrogen adsorption−desorption isotherm and pore size distributions for SCA−T. (d-e) FESEM images of SCA− 700. (f-g) TEM image and the corresponding EDS mappings for C, S, and O elements of SCA− 700.
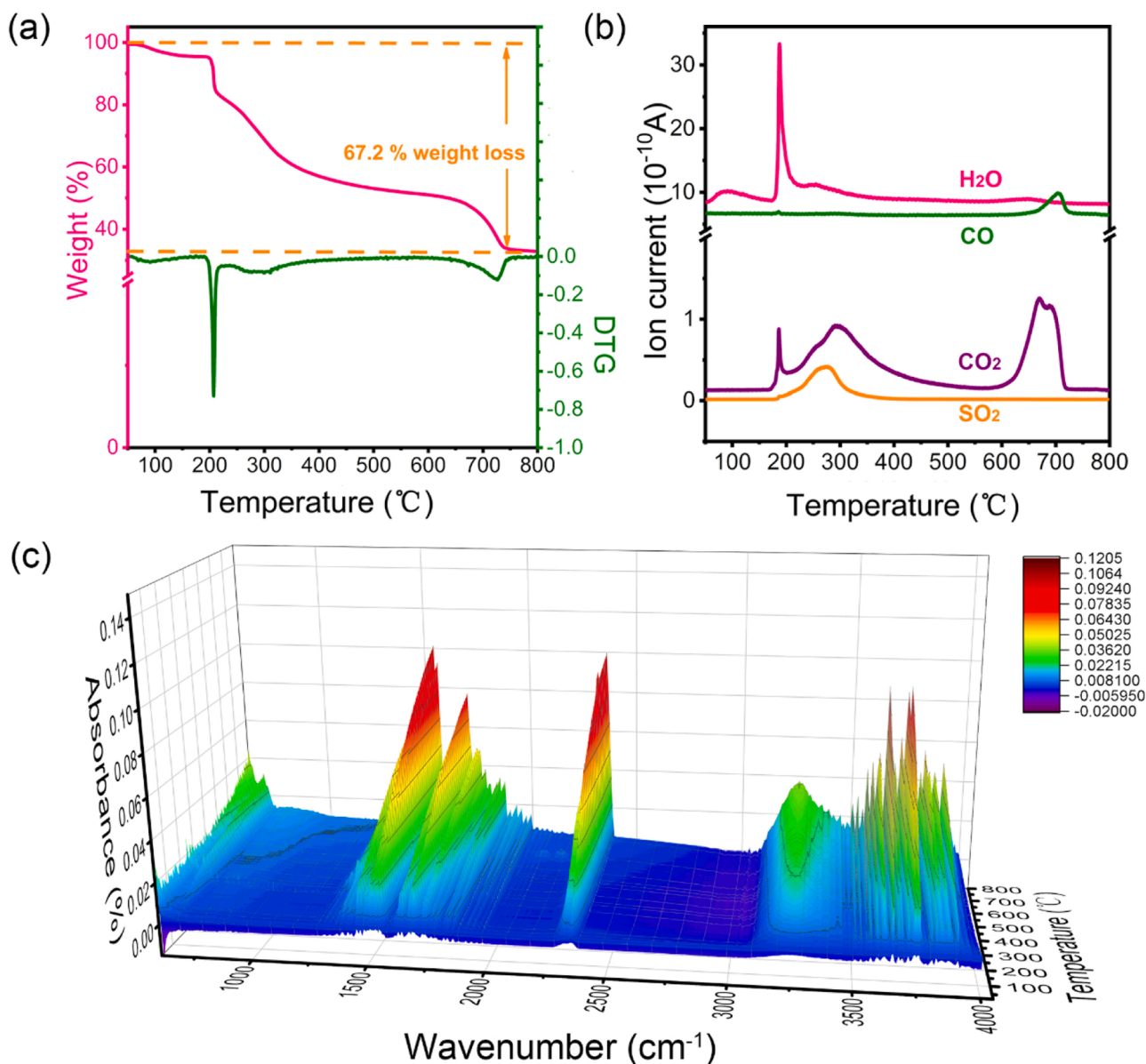
Fig. 3. (a) TGA and DTG curves of carrageenan aerogel in N_2 atmosphere. (b) The analysis of outlet gases from the decomposition of carrageenan aerogel TG-MS: H_2O (pink), CO (olive), CO_2 (purple) and SO_2 (orange). (c) 3D TG-FTIR spectra of carrageenan aerogel.

curves (CO_2 and CO) could be ascribed to the second (227 −380 °C) and third (672 −741 °C) major decomposition steps, respectively, corresponding to the TG curves. Thus, during the pyrolysis process, the oxygen-containing groups (−SO_4H, C−O−C and −OH et al.) in carrageenan molecular are converted to H_2O, CO_2, SO_2 and CO by the TG and TG−MS analysis. Based on the loss of SO_2, CO_2 and CO, it can be calculated that 11% of C and 4% of marine biogenic S are lost. Hence, the 89% of C and 96% of marine biogenic S are preserved in catalyst. In addition, the 3D TG−Fourier transform infrared spectriscopy spectra (TG−FTIR) was carried out to further confirm the volatiles components in the thermal decomposition of carrageenan aerogel. As shown in Fig. 3c, from the 3D TG−FTIR spectrum, the peaks at wavenumbers $3851 − 3253$ cm^{-1} indicated the existence of H_2O by the stretching vibration of O−H bonds [40]. The adsorption bands at $2400 − 2240$ cm^{-1} were assigned to CO_2 and CO. The peaks at wavenumber $1700 − 1600$ cm^{-1} and $1600 − 1520$ cm^{-1} were the stretching vibration of C=O bonds and C=C bonds, respectively, which confirms the existence of some carbonyl compounds (such as ketones, alkane, and acids) [41]. The peaks at wavenumbers 900–1131 cm^{-1} representing

the S=O bonds stretching vibration, which indicated the co-existence of oxidized S and sulfonate groups. In addition, at the wave number of 1200–1354 cm^{-1}, no peak was found in the original carrageenan, but with the increase of pyrolysis temperature, the C-S-C vibration peaks representing the thiophene-S structure began to appear [42].

3.4. XPS and XAS characterizations of SCA

The X − ray photoelectron spectroscopy (XPS) measurement of SCA− 700 was carried out to probe the chemical environments of C, S and O elements (Fig. 4a-b, Fig. S2). The peaks of C 1 s XPS spectrum at 284.4, 285 and 286.2 eV are related to C−S, C−C and C−O, respectively [43]. The O 1 s XPS spectrum can be split into three peaks at 531.3, 531.8 and 533.0 eV. The peak at 531.8 eV reveal the existence of SO_X species, while the other two peaks located at 531.3 and 533.0 eV are assigned to C=O and C−O−C, respectively [44]. As shown in high-−resolution S 2p spectra, the thiophene S (S $2p_{1/2}$ 163.7 and S $2p_{1/3}$ 165.1 eV) was determined to be the dominant S species [45]. The residual S located at 168.4 and 169.2 eV are attributed to the −C−SO_X
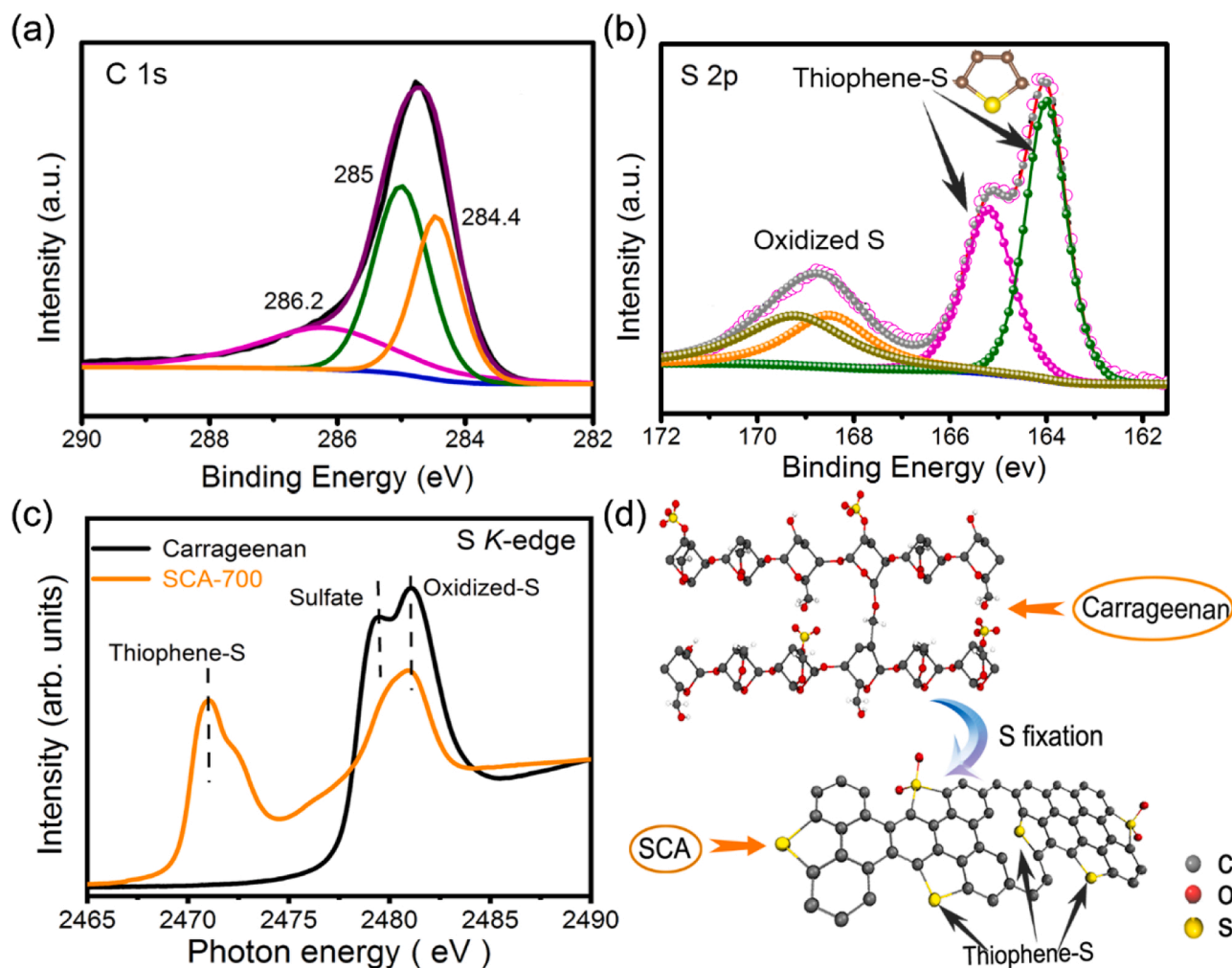
Fig. 4. (a-b) C 1 s and S 2p XPS spectra of SCA− 700. (c) S K-edge XAS spectra of carrageenan and SCA-700. (d) The schematic diagram of the process of the S fixation.

species [46,47]. Besides, the XPS of SCA− 600 and SCA− 800 were also tested. As shown in Fig. S3 and S4, compared with those of SCA− 700, the XPS peaks of C 1 s, O 1 s and S 2p for SCA− 600 and SCA− 800 have no obvious change, and the contents of C, S, and O are in the similar range (Table S3). Furthermore, the S K-edge X-ray absorption structure (XAS) spectra further confimed the existence of thiophene S structure. As shown in the Fig. 4c, the two major absorption bands are observed in the XAS of SCA-700 spectra, representing thiophene S (2471.1 eV) and oxidized-S (2481.1 eV), respectively [48]. However, in the XAS spectra of carrageenan, only sulfonate (2479.8 eV) and oxidized-S (2481.1 eV) are visible, which indicates that the sulfonate and oxidized-S in carrageenan were transformed or removed into thiophene S and oxidized-S after the fixation process [49]. The XPS and XAS results demonstrated that the contained S in carrageenan was successfully fixed in a carbon framework and converted to thiophene S and oxidized S (Fig. 4d).

3.5. The NRR activities of SCA

For NRR tests, we used the carbon paper coated with SCA−T as working electrode. The photograph of electrochemical setup for NRR test can be seen in the Fig. S5. Besides, the NH$_3$ yield rates and FEs were obtained by spectrophotometry with indophenol blue method (Fig. S6, Fig. S7) [50]. Fig. 5a shows the NRR performance of SCA−T in 0.1 M HCl electrolyte. Apparently, the sample of SCA− 700 exhibits much higher NH$_3$ yield rates than SCA− 600 and SCA− 800. Considering their similar S content, the high catalytic performance of SCA− 700 may be

more relevant to its higher specific surface area. Then, we measured the linear sweep voltammograms (LSVs) in Ar and N$_2$ −saturated 0.1 M HCl electrolyte to further appraise the NRR electrocatalytic activity of the most active SCA− 700 (Fig. 5b). Apparently, the current density under N$_2$ is higher than that under Ar, indicating the occurrence of eletrocatalytic N$_2$ reduction [51]. The chronoamperometry curves at different working potentials imply that as−prepared SCA− 700 can ensure the stability for reaction process (Fig. 5c) [52]. Fig. 5d displays the corresponding NH$_3$ yield rates and FEs of SCA− 700 under different potentials. The N$_2$ can be reduced to NH$_3$ at the potential of − 0.1 V to − 0.5 V (vs. RHE). Besides, both NH$_3$ yield rate and FE improve as the potential is negatively shifted, and achieve the highest value at the potential of − 0.3 V. The highest NH$_3$ yield rate and FE are 36.69 μg h^{-1} mg$_{cat}^{-1}$ and 8.72%, respectively. Obviously, the NH$_3$ yield rate of SCA-700 is higher than the most of the previously reported metal-free electrocatalysts (Fig. 5e and Table S2). In addition, to further confirm that the detected NH$_3$ was generated via the N$_2$ fixation process over SCA− 700, we also performed electrolysis in Ar−saturated solution, and pure carbon paper in N$_2$ −saturated solution at − 0.3 V for 2 h. The corresponding UV−Vis absorption spectra show no detectable NH$_3$ generated in either condition (Fig. S8). In addition, ion chromatography was used to analyze the n-saturated electrolyte before NRR test to ensure no contamination of nitrogen oxides (NO$_2^-$, NO$_3^-$). As shown in the Fig. S9, no signal of NO$_2^-$/NO$_3^-$ could be detected in the solution, which excluded the possibility of nitrogen oxide pollution in the catalytic environment and further demonstrated the reliability and authenticity of catalyst
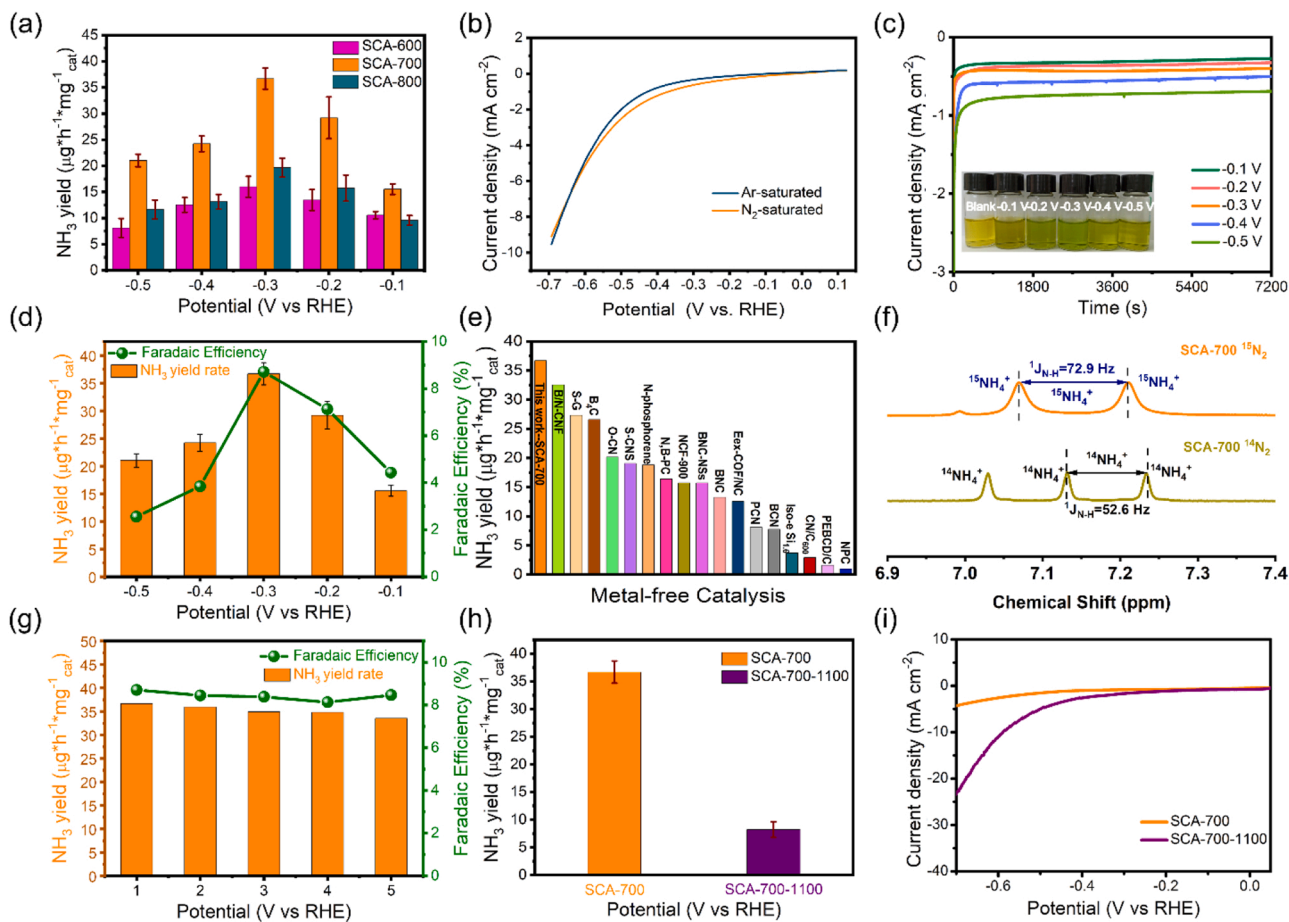
Fig. 5. (a) NH_3 yield of SCA−T in 0.1 M HCl electrolyte. (b) LSV curves of SCA− 700 in Ar−saturated and in N_2 −saturated electrolyte. (c) The corresponding chronoamperometry curves of SCA− 700 at different potentials in 0.1 M HCl solution. (d) NH_3 yield and FEs of SCA− 700 under different potentials. (e) Comparison of the NH_3 yield rate among SCA-700 and available reported metal-free catalysts. (f) ^1H NMR analysis of the electrolyte fed by $^{15}N_2$ and $^{14}N_2$ after electrolytic reaction at − 0.3 V. (g) Cycling test of SCA− 700 at − 0.3 V. (h) NH_3 yield and (i) HER performances of SCA− 700 and SCA− 700 − 1100.

NRR performance. Furthermore, we tested the ^1H NMR analysis of the electrolyte fed by $^{15}N_2$ and $^{14}N_2$ after electrolytic reaction at − 0.3 V to further determine the N source of produced NH_3. As shown in Fig. 5f, only doublet peaks of $^{15}NH_4^+$ and triplet peaks of $^{14}NH_4^+$ were found in the ^{15}N and ^{14}N saturated electrolyte, and the coupling constants of 72.9 Hz and 52.6 Hz correspond to the standard $^{15}NH_4^+$ and $^{14}NH_4^+$, indicating that N_2 is the only source of produced NH_3 by SCA–700 [53]. Notably, the N_2H_4 (by−product) could be detected by spectrophotometry with the method of Watt and Chrisp [54]. The detecting calibration curve of N_2H_4 is shown in Fig. S10. We failed to detect the production of N_2H_4 in N_2–saturated electrolyte (after charging at −0.3 V for 2 h), indicating that SCA− 700 is an electrocatalyst with excellent selectivity for NRR (Fig. S11). Then, we performed cycling and chronoamperometric tests of SCA− 700 in 0.1 M HCl media to study the stability of catalyst for practical. As shown in the Fig. 5 g, no obvious decline in NH_3 yield rate and FE of SCA− 700 after 5 times cycling tests. And after the NRR test lasted for 10 h, the SCA− 700 shows a relatively stable current density at − 0.3 V (Fig. S12). To explore the structural changes, XRD and XPS tests were performed on SCA− 700 after the NRR test cycling. As shown in the Fig. S13 and Fig. S14, compared to SCA-700 before NRR (Fig. 2a, Fig. 4a-b, Fig. S2), few changes were observed in the peaks of XRD and the C, S, and O XPS spectra of SCA-700 after NRR 5 times cycling test. It demonstrates the excellent stability of SCA-700 for NRR.

3.6. The role of S for NRR

In order to further emphasize the significance of the fixed S unit in N_2

fixation, we annealed the SCA− 700 at 1100 °C to remove S atoms in SCA, fabricating SCA− 700 − 1100. The XPS of SCA− 700 − 1100 was displayed in Fig. S15. Apparently, only very weak peaks are observed in S 2p spectra of SCA− 700 − 1100, indicating that most of S atoms are removed after the pyrolysis at 1100 °C. The atomic percentage of S content is largely reduced from 4.64% for SCA− 700–0.15% for SCA− 700 − 1100 (Table S3). Besides, the charge transfer resistance (R_{ct}) of SCA− 700 − 1100 is much higher than that of SCA− 700 (Fig. S16), indicating that the fixed S can improve the conductivity and fast the charge transport ability [55]. As shown in Fig. 5h, the SCA− 700 − 1100 only delivers a yield rate of 8.2 μg h^{-1} mg_{cat}^{-1}, much lower than SCA− 700. To explore more potential factors influencing the NRR activity, the surface area, porosity and defect concentration in the SCA− 700 − 1100 and SCA-700 were also investigated. As shown in Fig. S17, after sulfur removal, SCA− 700 − 1100 still retains a highly porous structure with a high BET surface area of 1490.9 m^2 g^{-1}, which is comparable to that of SCA− 700 (1668.9 m^2 g^{-1}). Raman spectra (Fig. S18) indicate that there is no significant change in the defect degree for SCA− 700 and SCA− 700 − 1100. These result indicates that the fixed S unit is most likely the origin of the boosted NRR performance in SCA− 700.

Given that HER is the primary competitive reaction of NRR, we tested the HER performances of SCA− 700 and SCA− 700 − 1100 in acid solution as well. Obviously, as shown in Fig. 5i, the SCA− 700 shows lower HER catalytic activity than SCA− 700 − 1100, which indicated that the fixed S unit is the key to inhibit HER activity and promote NRR activity. Besides, the HER reaction pathway on SCA− 700

was performed by the DFT calculations (Fig. S19). The large energy barrier of H adsorption further proves the poor HER performance of SCA− 700 [56]. However, as revealed by the XPS results, the prepared SCA-700 contains two types of S units, thiophene S and S oxides, which is difficult to verify experimentally which of the two S units is the main active species for catalytic N_2 reduction. Therefore, we compared the Gibbs free energy of N_2 protonation (ΔG_{NNH*}) of the two S units to determine the best active unit for NRR by DFT calculations. Apparently, compared with thiophene S (−0.37 eV), the oxidized S unit exhibits very high ΔG_{NNH*} of 2.43 eV in the N_2 protonation process, which means that the oxidized S unit is hard to active N_2, and is ineffective on electrocatalytic N_2 fixation (Fig. S20). Based on the above results, it can be concluded that the thiophene S unit is the main active site for N_2 fixation in SCA-700 electrocatalysts.

3.7. The NRR mechanism based on the DFT calculations

To reveal the role of thiophene S structure of SCA on NRR, we studied the electronic structure of SCA and the Gibbs free energy diagram of NRR on SCA by the DFT calculations. As shown in Fig. 6a, we constructed computational calculations on two types of models, pure carbon substrate (G) and thiophene S 5 −membered ring on carbon substrate (S−G). Firstly, we computed the adsorption energies (E_{ads}) of N_2 and intermediate NNH* at G and S-G surfaces, respectively (Fig. 6b). The computation results indicated that N_2 is adsorbed on the surface of G only by physical adsorption. The E_{ads} value of G is close to 0 eV, which indicated that N_2 is difficult to be adsorbed and activated by G at room tempreture. Oppositely, N_2 occurs on the surface of S-G via chemisorption with Eads value of − 0.43 eV, implying that N_2 can be easily adsorbed on S-G. Similarly, the Eads value of NNH on S-G is − 1.09 eV, which is much more negative than that on G (1.98 eV), indicating that S-G is more easily to adsorb NNH* . These results demonstrate that the thiophene S unit is critical factor to accelerate the adsorption of N_2 and NNH on carbon substrate [57]. The charge density difference is calculated to study the electron transfer behavior between N_2 and S−G or G. As shown in the top of Fig. 6c, there is no electron transfer between N_2 and G. In contrast, electron transfer occurs between N_2 and S−G, and 0.24 e^- is transferred from S-G to N_2. Due to the presence of thiophene S structure, S-G can "push" electrons into the antibonding orbitals of N_2, and simultaneously "pull" the lone-pair electrons from the N_2. Gibbs free energy of N_2 protonation (ΔG_{NNH*}) was calculated to highlight the effect of thiophene S for N_2 fixation (Fig. 6d). Apparently, the S−G exhibits
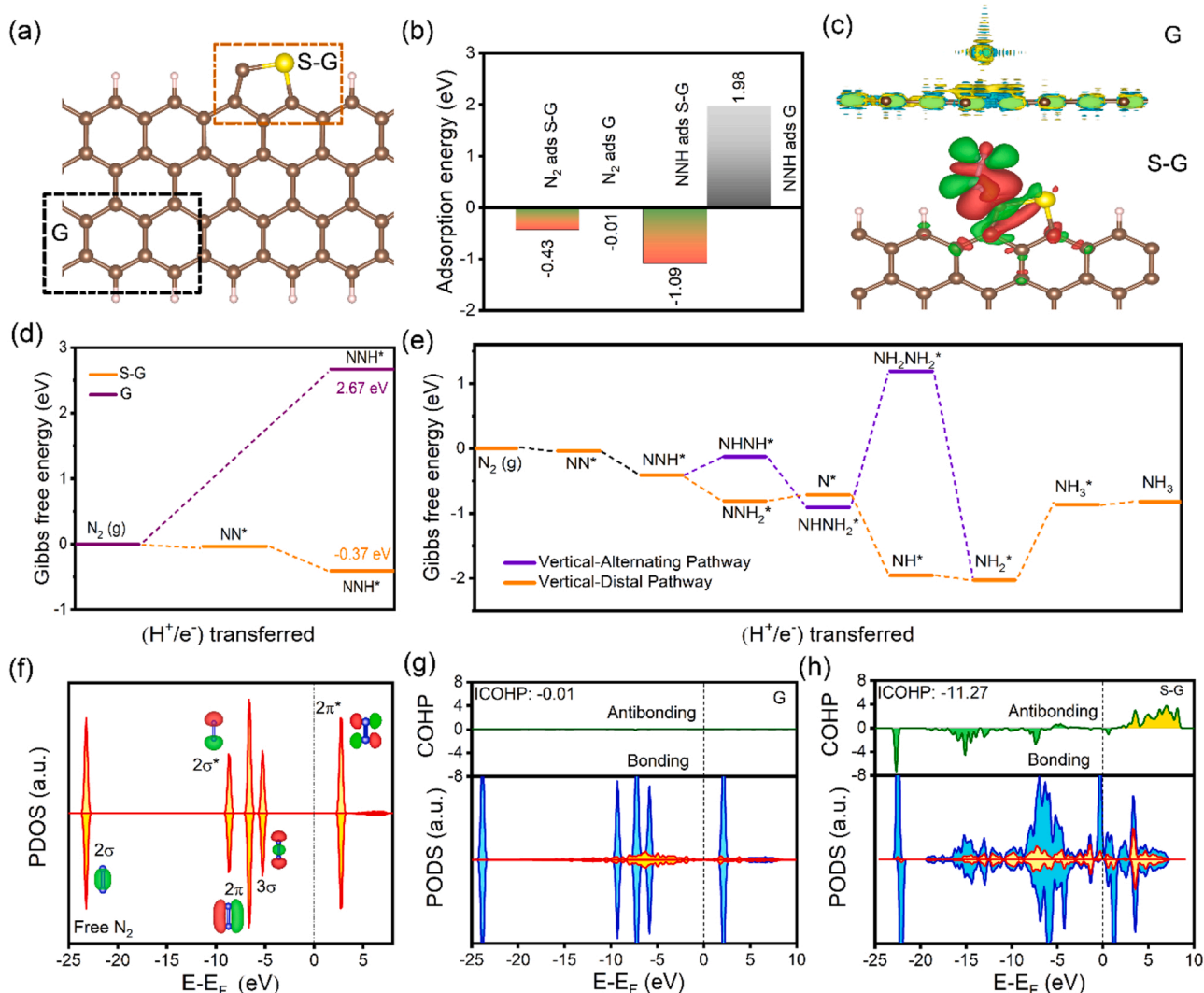
Fig. 6. (a) Schematic of computational models. Brown and yellow represent C and S atoms, respectively. (b) The adsorption energy of N_2 and NNH* on G and S-G surfaces. (c)The charge density difference at G and S−G. The red and cyan color represents the charge accumulation and depletion, respectively. (d) Calculated Gibbs free energy diagram of NNH* for G and S−G. (e) Gibbs free energy diagram of N_2 reduction on S−G. (f-h) Molecular orbitals of free N_2, and the computed partial density of states (PDOS) and the crystal orbital Hamilton populations (COHPs) of N_2 on G and S-G surfaces. The bonding and antibonding states in COHP are depicted by cyan and yellow, respectively.

much lower ΔG_{NNH^*} value (-0.37 eV) than G (2.67 eV), indicating that thiophene S can readily activate and protonate N_2. Thus, combining the above results, the presence of thiophene sulfur structure is critical factor to accelerate N_2 adsorption, dissociation and protonation on carbon substrate. As shown in Fig. 6e, we performed the possible reaction pathways for NH_3 synthesis on S−G. By contrast, the preferable pathway for NRR on S−G is N_2 (g) →NN* → NNH* → NNH_2 * → N * → NH* → NH_2 * → NH_3 * (distal pathway). The rate−determining step (RDS) of distal pathway is the generation of a second NH_3 (NH_2 * → NH_3 *). The energy barrier (1.15 eV) of RDS in distal pathway is much lower than that in alternating pathway (2.09 eV). The adsorption structure, total energy, reaction energy, zero-point energy, and entropy corrections of each intermediate were shown in the Supplementary Material (Fig. S21, Fig. S22, Table S4, Table S5). Therefore, the lowest energy barrier on S−G predicts that the SCA is an ideal electrocatalyst for catalyzing NRR.

To deep explore the underlying mechanism of N_2 activation, we analyzed the interactions between the S-G or G and N_2 by the plotting the partial density of states (PDOS) (Fig. 6f-h). Compared with the PDOS of free N_2 molecular, there is almost no interaction between G and N_2, nevertheless, the orbital energy levels of S-G and N_2 between $2\sigma^*$ and 3σ are well matched, indicating that S-G has strong interaction with N_2 [58]. Besides, we further performed the integrated-crystal orbital Hamilton population (ICOHP) analysis to more intuitively explore the positive effect of thiophene sulfur structure on N_2 adsorption. The ICOHP value of S-G is -11.27, which is much more negative than that of G (-0.01), indicating the strong adsorption capacity of S-G for N_2 [59]. As shown in the Fig. 6h, below the Fermi level, electrons are mostly filled in bonding orbitals rather than antibonding orbitals, indicating that S-G is strongly bounded to N_2, thus the thiophene S structure is favorable for the N_2 activation [60]. The results of PDOS and ICOHP are identical with those of Fig. 6b and d above, which further confirms the importance of thiophene S structure in adsorbing/activating N_2 and NRR.

4. Conclusion

In summary, we synchronously fix C and the carrageenan biogenic S into the SCA by using pyrolysis with the assistance of the unique hydrogel property of carrageenan, forming thiophene-S decorated biochar aerogel, which perfectly completes the role of C and S fixation. The resultant SCA exhibits excellent NRR activity and selectivity. Under ambient conditions, the yield rate of NH_3 and FE can reach 36.69 μg h^{-1} mg$_{cat}^{-1}$ and 8.72%, respectively, which exceeds mostly reported metal-free catalysis. DFT calculation results revealed that the thiophene S structure could accelerate adsorption and activation of N_2 by regulating the electronic structure of adjacent C atoms, and efficiently lower the energy barrier of the protonation of N_2. The preferable reaction pathway for NRR was N_2 (g) →NN* → NNH* → NNH_2 * → N * → NH* → NH_2 * → NH_3 * . This study opens up a new avenue for the synchronization fixation of marine biogenic S and C, and provides guidance and reference for the design of high-efficiency metal-free carbon-based NRR electrocatalyst.

Declaration of Competing Interest

The authors declare that they have no known competing financial interests or personal relationships that could have appeared to influence the work reported in this paper.

Acknowledgements

Appendix A. Supporting information

Supplementary data associated with this article can be found in the online version at doi:10.1016/j.apcatb.2022.121425.

References

[1] D. Dong, E. Du, Z. Sun, X. Zeng, W. Vries, Non-linear direct effects of acid rain on leaf photosynthetic rate of terrest plants, Environ. Pollut. 231 (2017) 1442–1445.
[2] F.C. Menz, H.M. Seip, Acid rain in Europe and the United States: an update, Energy Sci. Policy 7 (2004) 253–265.
[3] A.R.J. Curson, B.T. Williams, B.J. Pinchbeck, L.P. Sims, A.B. Martinez, P.P. L. Rivera, D. Kumaresan, E. Mercade, L.G. Spurgin, O. Carrion, S. Moxon, R. A. Cattolico, U. Kuzhiumparambil, P. Guagliardo, P.L. Clode, J.B. Raina, J.D. Todd, DSYB catalyses the key step of dimethylsulfoniopropionate biosynthesis in many phytoplankton, Nat. Microbiol 3 (2018) 430–439.
[4] R.C. Greene, Biosynthesis of d imethyl-β-propiothetin, J. Bio Chem. 237 (1962) 2251–2254.
[5] E. Ficko-Blean, A. Prechoux, F. Thomas, T. Rochat, R. Larocque, Y. Zhu, M. Stam, S. Genicot, M. Jam, A. Calteau, B. Viart, D. Ropartz, D. Pascual, G. Correc, M. Matard-Mann, K.A. Stubbs, H. Rogniaux, A. Jeudy, T. Barbeyron, C. Medigue, M. Czjzek, D. Vallenet, M.J. McBride, E. Duchaud, G. Michel, Carrageenan catabolism is encoded by a complex regulon in marine heterotrophic bacteria, Nat. Commun. 8 (2017) 1685.
[6] D. Li, D. Yang, X. Yang, Y. Wang, Z. Guo, Y. Xia, S. Sun, S. Guo, Double-helix structure in carrageenan–metal hydrogels: a general approach to porous metal sulfides/carbon aerogels with excellent sodium-ion storage, Angew. Chem. Int. Ed. 55 (2016) 15925–15928.
[7] J. Li, M. Du, G. Lv, L. Zhou, X. Li, L. Bertoluzzi, C. Liu, S. Zhu, J. Zhu, Interfacial solar steam generation enables fast-responsive, energy-efficient, and low-cost off-grid sterilization, Adv. Mater. 1 (2018) 1805159.
[8] W.J. Liu, H. Jiang, H. Yu, Emerging applications of biochar-based materials for energy storage and conversion, Energy Environ. Sci.. 12 (2019) 1751–1779.
[9] T. Zhang, Y. Liu, L. Yang, W. Li, W. Wang, P. Liu, Ti-Sn-Ce/bamboo biochar particle electrodes for enhanced electrocatalytic treatment of coking wastewater in a threedimensional electrochemical reaction system, J. Clean. Prod. 258 (2020), 120273.
[10] D. Li, C. Li, L. Zhang, H. Li, L. Zhu, D. Yang, Q. Fang, S. Qiu, X. Yao, Metal-free thiophene-sulfur covalent organic frameworks: precise and controllable synthesis of catalytic active sites for oxygen reduction, J. Am. Chem. Soc. 18 (2020) 8104–8108.
[11] D. Li, Y. Jia, G. Chang, J. Chen, H. Liu, J. Wang, Y. Hu, Y. Xia, D. Yang, X. Yao, A defect-driven metal-free electrocatalyst for oxygen reduction in acidic electrolyte, Chem 4 (2018) 2345–2356.
[12] L. Shi, Y. Yin, S. Wang, X. Xu, H. Wu, J. Zhang, S. Wang, H. Sun, Rigorous and reliable operations for electrocatalytic nitrogen reduction, Appl. Catal. B Environ. 227 (2020) 119325.
[13] X. Hu, Y. Sun, S. Guo, J. Sun, Y. Fu, S. Chen, S. Zhang, J. Zhu, Identifying electrocatalytic activity and mechanism of Ce$_{1/3}$NbO$_3$ perovskite for nitrogen reduction to ammonia at ambient conditions, Appl. Catal. B Environ. 280 (2021), 119419.
[14] K. Chu, Y. Luo, P. Shen, X. Li, Q. Li, Y. Guo, Unveiling the synergy of O-vacancy and heterostructure over MoO$_{3-x}$/MXene for N_2 electroreduction to NH_3, Adv. Energy Mater. 12 (2022), 2103022.
[15] X. Zhao, G. Hu, G. Chen, H. Zhang, S. Zhang, H. Wang, Comprehensive understanding of the thriving ambient electrochemical nitrogen reduction reaction, Adv. Mater. 33 (2021), 2007650.
[16] X. Li, Y. Luo, Q. Li, Y. Guo, K. Chu, Constructing an electron-rich interface over an Sb/Nb$_2$CT$_x$-MXene heterojunction for enhanced electrocatalytic nitrogen reduction, J. Mater. Chem. A. 9 (2021) 15955–15962.
[17] Y. Shi, Y. Liu, Vacancy and N dopants facilitated Ti^{3+} sites activity in 3D Ti$_{3-x}$C$_2$T$_y$ MXene for electrochemical nitrogen fixation, Appl. Catal. B Environ. 297 (2021), 120482.
[18] Y. Luo, Q. Li, Y. Tian, Y. Liu, K. Chu, Amorphization engineered VSe$_{2-x}$ nanosheets with abundant Se-vacancies for enhanced N_2 electroreduction, J. Mater. Chem. A. 10 (2022) 1742–1749.
[19] L. Xiao, S. Zhu, Y. Liang, Z. Li, S. Wu, S. Luo, C. Chang, Z. Cui, Effects of hydrophobic layer on selective electrochemical nitrogen fixation of self-supporting nanoporous Mo$_4$P$_3$ catalyst under ambient conditions, Appl. Catal. B Environ. 286 (2021), 119895.
[20] X. Lv, Y. Liu, Y. Wang, X. Liu, Z. Yuan, Encapsulating vanadium nitride nanodots into N, S-codoped graphitized carbon for synergistic electrocatalytic nitrogen reduction and aqueous Zn-N_2 battery, Appl. Catal. B Environ. 280 (2021), 119434.
[21] L. Li, C. Tang, X. Cui, Y. Zheng, X. Wang, H. Xu, S. Zhang, T. Shao, K. Davey, S. Qiao, Efficient nitrogen fixation to ammonia through integration of plasma oxidation with electrocatalytic reduction, Angew. Chem. Int. Ed. 60 (2021) 14131–14137.
[22] B. Chang, L. Li, D. Shi, H. Jiang, Z. Ai, S. Wang, Y. Shao, J. Shen, Y. Wu, Y. Li, X. Hao, Metal-free boron carbonitride with tunable boron Lewis acid sites for

enhanced nitrogen electroreduction to ammonia, Appl. Catal. B Environ. 283 (2021), 119622.

[23] W. Liang, W. Qin, D. Li, Y. Wang, W. Guo, Y. Bi, Y. Sun, L. Jiang, Localized surface plasmon resonance enhanced electrochemical nitrogen reduction reaction, Appl. Catal. B Environ. 301 (2022) 120808.

[24] L. Zhang, M. Cong, D. Xin, Y. Jin, F. Xu, Y. Wang, L. Chen, L. Zhang, A janus Fe-SnO₂ catalyst that enables bifunctional electrochemical nitrogen fixation, Angew. Chem. Int. Ed. 59 (2020) 10888–10893.

[25] H. He, Q. Zhu, Y. Yan, H. Zhang, Z. Han, H. Sun, J. Chen, C. Li, Z. Zhang, M. Du, Metal–organic framework supported Au nanoparticles with organosilicone coating for high-efficiency electrocatalytic N₂ reduction to NH₃, Appl. Catal. B Environ. 302 (2022), 120840.

[26] Q. Li, P. Shen, Y. Tian, X. Li, K. Chu, Metal-free BN quantum dots/graphitic C₃N₄ heterostructure for nitrogen reduction reaction, J. Colloid Interface Sci. 606 (2022) 204–212.

[27] M. Yuan, Q. Li, J. Zhang, J. Wu, T. Zhao, Z. Liu, L. Zhou, H. He, B. Li, G. Zhang, Engineering surface atomic architecture of NiTe nanocrystals toward efficient electrochemical N₂ fixation, Adv. Funct. Mater. 30 (2020), 2004208.

[28] Q. Li, Y. Guo, Y. Tian, W. Liu, K. Chu, Activating VS₂ basal planes for enhanced NRR electrocatalysis: the synergistic role of S-vacancies and B dopants, J. Mater. Chem. A. 8 (2020) 16195–16202.

[29] K. Chu, Q. Li, Y. Liu, J. Wang, Y. Cheng, Filling the nitrogen vacancies with Sulphur dopants in graphitic C₃N₄ for efficient and robust electrocatalytic nitrogen reduction, Appl. Catal. B Environ. 267 (2020) 118693.

[30] K. Chu, X. Li, Q. Li, Y. Guo, H. Zhang, Synergistic enhancement of electrocatalytic nitrogen reduction over boron nitride quantum dots decorated Nb₂CTₓ-MXene, Small 17 (2021), 2102363.

[31] Y. Wan, J. Xu, R. Lv, Heterogeneous electrocatalysts design for nitrogen reduction reaction under ambient conditions, Mater. Today 27 (2019) 69–90.

[32] M. Fauziyah, W. Widiyastuti, H. Setyawan, Nitrogen-doped carbon aerogels prepared by direct pyrolysis of cellulose aerogels derived from coir fibers using an ammonia-urea system and their electrocatalytic performance toward the oxygen reduction reaction, Ind. Eng. Chem. Res. 59 (2020) 21371–21382.

[33] M. Yu, Y. Han, J. Li, L. Wang, Magnetic N-doped carbon aerogel from sodium carboxymethyl cellulose/collagen composite aerogel for dye adsorption and electrochemical supercapacitor, Int. J. Biol. Macromol. 115 (2018) 185–193.

[34] S. Liu, M. Wang, T. Qian, H. Ji, J. Liu, C. Yan, Facilitating nitrogen accessibility to boron-rich covalent organic frameworks via electrochemical excitation for efficient nitrogen fixation, Nat. Commun. 10 (2019) 3898–3906.

[35] P. Song, H. Wang, L. Kang, B. Ran, H. Rong, R. Wang, Electrochemical nitrogen reduction to ammonia at ambient conditions on nitrogen and phosphorus co-doped porous carbon, Chem. Commun. 55 (2019) 687–690.

[36] R. Guo, D. Li, C. Lv, Y. Wang, H. Zhang, Y. Xia, D. Yang, X. Zhao, Porous Ni₃S₄/C aerogels derived from carrageenan-Ni hydrogels for high-performance sodium-ion batteries anode, Electrochim. Acta 10 (2019) 72–79.

[37] D. Li, C. Lv, L. Liu, Y. Xia, X. She, S. Guo, D. Yang, Egg-box structure in cobalt alginate: a new approach to multifunctional hierarchical mesoporous N-doped carbon nanofibers for efficient catalysis and energy storage, ACS Cent. Sci. 1 (2015) 261–269.

[38] L. Liu, X. Yang, N. Ma, H. Liu, Y. Xia, C. Chen, D. Yang, X. Yao, Scalable and cost-effective synthesis of highly efficient Fe₂N-based oxygen reduction catalyst derived from seaweed biomass, Small 10 (2016) 1295–1301.

[39] C. Lv, C. Yan, G. Chen, Y. Ding, J. Sun, Y. Zhou, G. Yu, An amorphous noble-metal-free electrocatalyst that enables nitrogen fixation under ambient conditions, Angew. Chem. Int. Ed. 57 (2018) 6073–6076.

[40] X. Chen, H. Sun, J. Zhang, Y. Guo, D. Kuo, Cationic S-doped TiO₂/SiO₂ visible-light photocatalyst synthesized by co-hydrolysis method and its application for organic degradation, J. Mol. Liq. 273 (2019) 50–57.

[41] D. Li, Y. Wang, Y. Sun, Y. Lu, S. Chen, B. Wang, H. Zhang, Y. Xia, D. Yang, Turning Gelidium amansii residue into nitrogen-doped carbon nanofiber aerogel for enhanced multiple energy storage, Carbon 137 (2018) 31–40.

[42] G. Mishra, K.M. Parida, S.K. Singh, Facile fabrication of S-TiO₂/β-SiC nanocomposite photocatalyst for hydrogen evolution under visible light irradiation, ACS Sustain. Chem. Eng. 3 (2015) 245–253.

[43] X. Cheng, F. Ran, Y. Huang, R. Zheng, H. Yu, J. Shu, Y. Xie, Y. He, Insight into the synergistic effect of N, S Co-doping for carbon coating layer on niobium oxide anodes with ultra-long life, Adv. Funct. Mater. 31 (2021), 2100311.

[44] L. Xing, K. Xi, Q. Li, Z. Su, C. Lai, X. Zhao, R.V. Kumar, Nitrogen, sulfur-codoped graphene sponge as electroactive carbon interlayer for high-energy and -power lithium–sulfur batteries, J. Power Sources 303 (2016) 22–28.

[45] Y. Su, Z. Yao, F. Zhang, H. Wang, Z. Mics, E. Cánovas, M. Bonn, X. Zhuang, X. Feng, Sulfur-enriched conjugated polymer nanosheet derived sulfur and nitrogen co-doped porous carbon nanosheets as electrocatalysts for oxygen reduction reaction and zinc–air battery, Adv. Funct. Mater.. 26 (2016) 5893–5902.

[46] W. Qian, J. Zhu, Y. Zhang, X. Wu, F. Yan, Condiment-derived 3D architecture porous carbon for electrochemical supercapacitors, Small 37 (2015) 4959–4969.

[47] J. Farideh, Sulfur: not a "silent" element any more, Chem. Soc. Rev. 35 (2006) 1256–1268.

[48] A. Vairavamurthy, Using X-ray absorption to probe sulfur oxidation states incomplex molecules, Spectrochim. Acta Part A 54 (1998) 2009–2017.

[49] J.R. Han, Z. Liu, Y. Ma, G. Cui, F. Xie, F. Wang, Y. Wu, S. Gao, Y. Xu, X. Sun, Ambient N₂ fixation to NH₃ at ambient conditions: Using Nb₂O₅ nanofiber as a high-performance electrocatalyst, Nano Energy 52 (2018) 264–270.

[50] L. Xia, J. Yang, H. Wang, R. Zhao, H. Chen, W. Fang, A.M. Asiri, F. Xie, G. Cui, X. Sun, Sulfur-doped graphene for efficient electrocatalytic N₂-to-NH₃ fixation, Chem. Commun. 55 (2019) 3371–3374.

[51] Y. Zhang, Q. Zhang, D. Liu, Z. Wen, J. Yao, M. Shi, Y. Zhu, J. Yan, Q. Jiang, High spin polarization ultrafine Rh nanoparticles on CNT for efficient electrochemical N₂ fixation to ammonia, Appl. Catal. B Environ. 298 (2021), 120592.

[52] Y. Ren, C. Yu, X. Tan, H. Huang, Q. Wei, J. Qiu, Strategies to suppress hydrogen evolution for highly selective electrocatalytic nitrogen reduction: challenges and perspectives, Energy Environ. Sci. 14 (2021) 1176–1193.

[53] S.Z. Andersen, V. Čolić, S. Yang, J.A. Schwalbe, A.C. Nielander, J.M. McEnaney, K. Enemark-Rasmussen, J.G. Baker, A.R. Singh, B.A. Rohr, M.J. Statt, S.J. Blair, S. Mezzavilla, J. Kibsgaard, P.C.K. Vesborg, M. Cargnello, S.F. Bent, T.F. Jaramillo, I.E.L. Stephens, J.K. Nørskov, Chorkendorff, A rigorous electrochemical ammonia synthesis protocol with quantitative isotope measurements, Nature 570 (2019) 504–508.

[54] W. Zhang, Y. Zou, H. Liu, S. Chen, X. Wang, H. Zhang, X. She, D. Yang, Single-crystalline (FeₓNi₁₋ₓ)₂P nanosheets with dominant {01$\overline{1}$1} facets: efficient electrocatalysts for hydrogen evolution reaction at all pH values, Nano Energy 56 (2019) 813–822.

[55] G. Chang, J. Ren, X. She, K. Wang, S. Komarneni, D. Yang, How heteroatoms (Ge, N, P) improve the electrocatalytic performance of graphene: theory and experiment, Sci. Bull. 63 (2018) 155–158.

[56] K.W. Wang, X. She, S. Chen, H. Liu, D. Li, Y. Wang, H. Zhang, D. Yang, X. Yao, Boosting hydrogen evolution via optimized hydrogen adsorption at the interface of CoP₃ and Ni₂P, J. Mater. Chem. A 6 (2018) 5560–5565.

[57] Q. Li, X. Wang, K. Tang, M. Wang, C. Wang, C. Yan, Electronic modulation of electrocatalytically active center of Cu₇S₄ nanodisks by Cobalt-doping for highly efficient oxygen evolution reaction, ACS Nano 11 (2017) 12230–12239.

[58] X. Guo, J. Gu, S. Lin, S. Zhang, Z. Chen, S. Huang, Tackling the activity and selectivity challenges of electrocatalysts toward the nitrogen reduction reaction via atomically dispersed biatom catalysts, J. Am. Chem. Soc. 142 (2020) 5709–5721.

[59] S. Maintz, V.L. Deringer, A.L. Tchougréeff, R. Dronskowski, LOBSTER: a tool to extract chemical bonding from plane-wave based DFT, J. Comput. Chem. 37 (2016) 1030–1035.

[60] C. Ling, Y. Ouyang, Q. Li, X. Bai, X. Mao, A. Du, J. Wang, A general two-step strategy-based high-throughput screening of single atom catalysts for nitrogen fixation, Small Methods 3 (2019) 1800376–1800383.